Editors' Suggestion

Sum-frequency ionic Raman scattering

Dominik M. Juraschek[1,*] and Sebastian F. Maehrlein[2,3]
[1]*Materials Theory, ETH Zurich, CH-8093 Zürich, Switzerland*
[2]*Department of Physical Chemistry, Fritz Haber Institute of the Max Planck Society, DE-14195 Berlin, Germany*
[3]*Department of Chemistry, Columbia University, New York, New York 10027, USA*

(Received 31 January 2018; published 16 May 2018)

In a recent report, sum-frequency excitation of a Raman-active phonon was experimentally demonstrated. This mechanism is the sibling of impulsive stimulated Raman scattering, in which the difference-frequency components of a light field excite a Raman-active mode. Here, we propose that also *ionic* Raman scattering analogously has a sum-frequency counterpart. We compare the four Raman mechanisms, photonic and ionic difference- and sum-frequency excitation, for three different example materials using a generalized oscillator model for which we calculate the parameters with density functional theory. Sum-frequency ionic Raman scattering completes the toolkit for controlling material properties by means of selective excitation of lattice vibrations.

DOI: 10.1103/PhysRevB.97.174302

I. INTRODUCTION

Ultrashort electromagnetic pulses are an established tool to control the electronic and structural phases of matter. Intense laser pulses in the terahertz spectral range provide direct access to the excitation of optical phonons and have become practical only during the past decade [1–4]. Highly excited optical phonons govern a variety of physical phenomena, such as phase transitions [5], induced or enhanced superconductivity [6–8], and control of magnetic order [9,10]. It is therefore necessary to understand the fundamental mechanisms that underlie the excitation of coherent optical phonons with light. Infrared-active phonons carry an electric-dipole moment and can therefore be excited directly by coupling to the electric field component of electromagnetic radiation. For Raman-active phonons, which do not possess an electric-dipole moment, another, indirect way has to be taken.

An established route is to disturb the electronic system with an ultrashort light pulse, which then mediates energy to Raman-active phonons via electron-phonon interactions [11,12]. For coherent, nonresonant excitations below the band gap [13], the primary mechanism involved is impulsive stimulated Raman scattering (ISRS), in which a virtual electronic state serves as the intermediate energy level for the Raman scattering of the incident light by the phonon [see Fig. 1(a)] [14–16]. In this case, the difference frequency of two photons from the light pulse is resonant with a vibrational transition of the phonon mode. In the following, we will refer to this as a "photonic" Raman mechanism.

A second route to exciting Raman-active phonons is via scattering with infrared-active phonons. This was proposed nearly half a century ago as an ionic Raman scattering process and has only been demonstrated within this decade due to the advancement of intense terahertz sources [17–20]. In this process, an infrared-active phonon, which is coherently excited by light, serves as the intermediate state for Raman scattering [see Fig. 1(b)]. This effect is mediated through anharmonic phonon-phonon coupling rather than electron-phonon interactions, and it is less dissipative than its photonic counterpart due to the lower energy of the excitation [21,22]. In the following, we will refer to this specific mechanism simply as ionic Raman scattering (IRS). Note that there are also other types of ionic Raman scattering, which involve higher-order processes in the electric-dipole or phonon-phonon interaction [19].

In a recent experiment, a third route has been demonstrated, in which the 40 THz Raman-active phonon of diamond is excited by a terahertz pulse in a two-photon absorption process [see Fig. 1(c)] [23]. This is the sum-frequency excitation (SFE) counterpart to ISRS, which combines the possibility to excite phonons in compounds that do not possess infrared-active phonons with the advantage of low-energy excitation by terahertz radiation.

The purpose of this theoretical study is twofold: First, we complete the map of photonic and ionic difference- and sum-frequency Raman mechanisms with the "missing" sum-frequency part of ionic Raman scattering (SF-IRS) that is tantamount to the absorption of two coherently excited infrared-active phonons by a Raman-active phonon [see Fig. 1(d)]. Second, we compare the four mechanisms for three different example materials: diamond, erbium ferrite ($ErFeO_3$), and bismuth ferrite ($BiFeO_3$). This includes also a theoretical confirmation and quantitative description of THz-SFE by means of first-principles calculations. Assuming realistic experimental conditions, we show that sum-frequency excitations, both photonic and ionic, are able to coherently control Raman-active phonons in the electronic ground state in a way that is complementary to previous nonlinear phononics studies.

II. THEORETICAL MODEL

A. General equation of motion for the excitation of phonons

To investigate the time evolution of a phonon mode we numerically solve its equation of motion,

$$\ddot{Q} + \kappa \dot{Q} + \frac{\partial}{\partial Q} V(Q) = \sum_i Z_i E_i + \varepsilon_0 \sum_{ij} R_{ij} E_i E_j, \quad (1)$$

*Corresponding author: dominik.juraschek@mat.ethz.ch

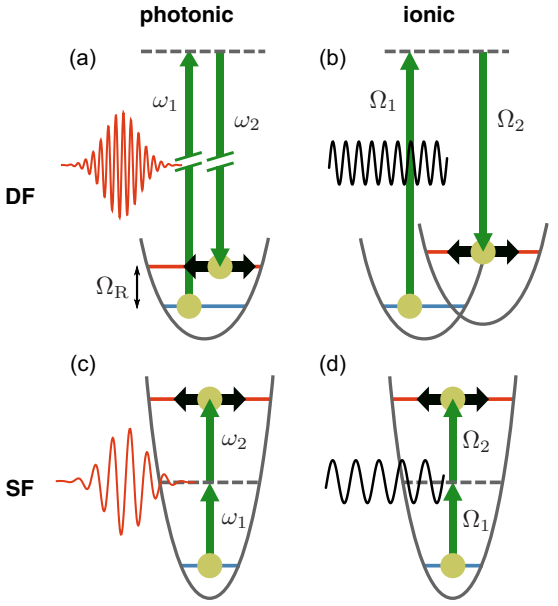

FIG. 1. Map of photonic and ionic Raman mechanisms. The difference- and sum-frequency components of a light pulse, $\omega_1 \pm \omega_2$, or a coherently excited infrared-active phonon, $\Omega_1 \pm \Omega_2$, are resonant with a vibrational transition of a Raman-active phonon Ω_R. (a) Impulsive stimulated Raman scattering (ISRS). (b) Conventional ionic Raman scattering (DF-IRS). The lattice potential of the Raman-active mode shifts. (c) Terahertz sum-frequency excitation (THz-SFE). (d) Proposed sum-frequency counterpart of ionic Raman scattering (SF-IRS).

where Q is the normal mode coordinate (or amplitude) of the phonon at the Brillouin-zone center in units of $\sqrt{\mu}$Å, with μ being the atomic mass unit. κ is the phonon linewidth, and $V(Q)$ is the (an)harmonic lattice potential of the phonon. E_i is the electric field component of the exciting electromagnetic pulse, and the indices i and j run over the spatial coordinates. $Z_i = (\sum_n \mathbf{Z}_n^* \mathbf{u}_n)_i$ is the mode effective charge of the phonon with $\mathbf{Z}_n^*$ being the Born effective charge tensor and $\mathbf{u}_n$ the displacement vector of atom n, and the sum runs over all atoms in the unit cell [24]. $R_{ij} = V_c \partial_Q \chi_{ij}$ is the Raman tensor, which is given by the linear electric susceptibility χ_{ij} and the volume of the unit cell V_c. Phonon linewidths lie in the range of $\kappa \approx \Omega/10$ to $\Omega/20$ for the materials that we consider here, where Ω is the eigenfrequency of the phonon mode [9,23,25]. For a detailed derivation, see, for example, Ref. [26]. We model the electric field component of a light or terahertz pulse as $E(t) = E_0 \exp\{-(t - t_0)^2/[2(\tau/\sqrt{8\ln 2})^2]\} \cos(\omega_0 t + \varphi_{CEP})$, where E_0 is the peak electric field, ω_0 is the center frequency, φ_{CEP} is the carrier-envelope phase, and τ is the full width at half maximum duration of the pulse.

B. Equations of motion for photonic and ionic Raman scattering

For photonic Raman scattering we assume a harmonic lattice potential $V(Q_R) = \Omega_R^2 Q_R^2/2$, as anharmonicities are not important for the process. Furthermore, in centrosymmetric crystals, $Z_i = 0$ for Raman-active phonons, and for a linearly polarized laser pulse, we can write Eq. (1) as

$$\ddot{Q}_R + \kappa_R \dot{Q}_R + \Omega_R^2 Q_R = \varepsilon_0 R E^2(t). \quad (2)$$

In contrast, ionic Raman scattering is described by a quadratic-linear coupling of an infrared-active with a Raman-active phonon. The anharmonic lattice potential in its simplest form can be expressed as $V(Q_R, Q_{IR}) = \Omega_R^2 Q_R^2/2 + \Omega_{IR}^2 Q_{IR}^2/2 + c Q_{IR}^2 Q_R$, where c is the quadratic-linear coupling coefficient given in meV/$(\sqrt{\mu}\text{Å})^3$ [21]. We have to solve the equations of motion for both phonons, and Eq. (1) can be written respectively as

$$\ddot{Q}_{IR} + \kappa_{IR} \dot{Q}_{IR} + \left(\Omega_{IR}^2 + 2c Q_R\right) Q_{IR} = Z_{IR} E(t), \quad (3)$$

$$\ddot{Q}_R + \kappa_R \dot{Q}_R + \Omega_R^2 Q_R = c Q_{IR}^2(t). \quad (4)$$

The driving force of the Raman-active phonon in photonic Raman scattering is the square of the electric field $E^2(t)$ [see Eq. (2)], while in ionic Raman scattering it is the square of the "phonon field" of the infrared-active phonon $Q_{IR}^2(t)$ [see Eq. (4)]. In addition, the Raman-active mode feedback affects the initially excited infrared-active mode by dynamically renormalizing its frequency as $\Omega_{IR}^2 \rightarrow \Omega_{IR}^2 + 2c Q_R$ [see Eq. (3)].

The two photonic processes, ISRS and THz-SFE, can be described by the same equation of motion (2). The two mechanisms are only distinguished by the duration of the pulse and its center frequency ω_0, which is higher than the phonon frequency in ISRS, $\omega_0 > \Omega_R$, and ideally half the phonon frequency in THz-SFE, $\omega_0 = \Omega_R/2$. We can draw an analogy for ionic Raman scattering here, which has so far been always connected to the coupling of a high-frequency infrared-active phonon with a low-frequency Raman-active phonon, $\Omega_{IR} > \Omega_R$, in which the difference-frequency components of the phonon field Q_{IR}^2 are responsible for the excitation of the Raman-active phonon [20,21,27–34]. Here, we will show that this mechanism can be extended to a sum-frequency counterpart that fulfills $\Omega_{IR} = \Omega_R/2$, analog to the photonic Raman processes [23]. A summary of the discussion in this section is given in Table I, in which also the results for phase sensitivity and impulsiveness from the following sections are shown.

TABLE I. Summary of properties of the four mechanisms for the excitation of Raman-active phonons in insulators.

	ISRS	DF-IRS	THz-SFE	SF-IRS
Type of excitation	Photonic	Ionic	Photonic	Ionic
Driving force	$E^2(t)$	$Q_{IR}^2(t)$	$E^2(t)$	$Q_{IR}^2(t)$
Center frequency	$\omega_0 > \Omega_R$	$\Omega_{IR} > \Omega_R$	$\omega_0 = \Omega_R/2$	$\Omega_{IR} = \Omega_R/2$
Frequency components	Difference	Difference	Sum	Sum
CEP sensitive	No	No	Yes	Yes
Impulsive	Yes	Yes	No	No

C. Computational details

We calculated the phonon eigenfrequencies, eigenvectors, and the Raman tensors from first principles using the density functional theory formalism as implemented in the Vienna *ab initio* simulation package (VASP) [35,36], and the frozen-phonon method as implemented in the PHONOPY package [37]. To calculate the frequency-dependent Raman tensor we followed the scheme of Ref. [38]. We used the default VASP projector augmented-wave (PAW) pseudopotentials for every considered atom and converged the Hellmann-Feynman forces to 10^{-5} eV/Å using a plane-wave energy cutoff of 950 eV and a $9 \times 9 \times 9$ k-point Monkhorst-Pack mesh [39] to sample the Brillouin zone for diamond and 850 eV, $6 \times 6 \times 6$ for $BiFeO_3$. For the exchange-correlation functional, we chose the Perdew-Burke-Ernzerhof revised for solids (PBEsol) form of the generalized gradient approximation (GGA) [40]. For $BiFeO_3$ we found that an on-site Coulomb interaction of 4 eV and a Hund's exchange of 1 eV optimally reproduce both the G-type antiferromagnetic ordering and lattice dynamical properties [41,42]. Our fully relaxed structures with lattice constants 3.55 Å for diamond and 3.94 Å with a pseudocubic angle of 90.44° for $BiFeO_3$ fit reasonably well to common experimental values [43,44], as do our calculated phonon frequencies. Our calculated phonon eigenfrequency for the F_{2g} mode in diamond is 39.2 THz, though for simplicity we keep referring to it as the "40 THz mode." For the details on $ErFeO_3$, we refer the reader to the computational details of Ref. [25].

III. RESULTS

A. THz-SFE vs ISRS in diamond

We begin by reproducing the experiments of Refs. [23,45], in which the 40 THz F_{2g} Raman-active phonon of diamond was excited via THz-SFE and ISRS, respectively. Both mechanisms can be described by Eq. (2), for which we use the experimental excitation pulses with a center frequency of $\omega_0/2\pi = 20$ THz and pulse duration of $\tau = 0.2$ ps for the terahertz pulse for THz-SFE, and $\omega_0/2\pi = 759$ THz (395 nm) and $\tau = 10$ fs for the visible light pulse for ISRS. The electric field is oriented along the Raman-active [110] direction with a peak electric field of $E_0 = 8$ MV/cm in both cases. The calculated parameters for the equation of motion are given in Table II, and the eigenvector of the F_{2g} mode is illustrated in Fig. 2(a). Our first-principles calculations allow us to determine the single independent component of the Raman tensor for frequencies throughout and up to slightly above the electronic band gap. Figure 2(b) shows that for large band-gap materials, the frequency dependence of the Raman tensor does not play a significant role when comparing Raman effects in the visible- and terahertz spectral range, setting ISRS and THz-SFE on equal footing. Further, electronic excitations, which are described by the imaginary part of the Raman tensor, are negligible for the photon energies we use in the examples here [16].

TABLE II. Calculated phonon frequencies of the infrared- and Raman-active modes Ω_{IR} and Ω_R, mode effective charge of the infrared-active mode Z_{IR}, Raman tensor at the respective visible and terahertz frequencies of the laser pulses $R(\omega)$, and quadratic-linear coupling coefficient c.

Quantity	Diamond	$ErFeO_3$	$BiFeO_3$
Ω_{IR} | Ω_R (THz)	– | 39.2	16.5 | 3.2	7.4 | 15.3
Z_{IR} $(e/\sqrt{\mu})$		0.67	0.82
R (VIS) $(Å^2/\sqrt{\mu})$	70		
R (THz) $(Å^2/\sqrt{\mu})$	50	−9	−41
c (meV/(Å$\sqrt{\mu})^3$)		7.8	8.0

We show the resulting dynamics of the F_{2g} mode for the two different optical excitations as described by Eq. (2) in Fig. 2(c). For THz-SFE, the response shows a gradual increase of the phonon amplitude with the onset of the terahertz pulse, which illustrates that the mechanism is nonimpulsive. The maximum phonon amplitude reaches $Q = 0.28 \times 10^{-2}\sqrt{\mu}$Å, and the phase of the oscillation is sensitive to the carrier-envelope phase of the terahertz pulse φ_{CEP} [46]. These results reproduce the essential features of the experiment in Ref. [23] and give a quantitative estimate of the THz-SFE induced phonon amplitude. In contrast, the response for ISRS shows an abrupt onset of the phonon amplitude at $t = 0$, which is characteristic for the impulsive nature of the mechanism. The maximum phonon amplitude reaches $Q = 0.04 \times 10^{-2}\sqrt{\mu}$Å, and the phase of the oscillation is independent of φ_{CEP} [46]. These results reproduce the essential features of the experiment in Ref. [45] and agree well with the results of recent time-dependent density functional theory studies for ISRS [47,48].

Despite the smaller value of the Raman tensor R(THz) compared to R(VIS) [see Table II and Fig. 2(b)], THz-SFE is roughly one order of magnitude stronger than ISRS for a similar peak electric field E_0. This is because the 40 THz frequency component of the driving force $E^2(t)$, resulting from the sum frequency of the 20 THz pulse, is roughly a factor of ten higher than that resulting from the difference frequency of the 395 nm pulse. This order-of-magnitude difference in excitation strength persists for pulses throughout the visible spectrum [46].

To take into account the total pulse energy, we show the dependence of the coherent phonon amplitude on the duration of the pump pulse in Fig. 2(d) for two distinct cases: (i) constant peak field E_0 and (ii) constant pulse energy. In ISRS there is an optimal value of pulse duration for constant E_0 that corresponds to a bandwidth of the pulse, for which the difference-frequency components at 40 THz are maximal. When the energy of the pulse is fixed, a shorter pulse will trade off for a higher E_0 and therefore increase the effect until the pulse gets too short and approaches the single cycle regime. For THz-SFE the situation is different: Due to its nonimpulsive nature, a longer duration of the pulse will continuously increase the coherent phonon amplitude, when E_0 is kept constant. In this case, the amplitude will build up until damping κ and the excitation force are balanced. In contrast, keeping the total pulse energy constant, a longer pulse will trade off for a lower E_0 and the effect decreases. Note that our model does not include terahertz absorption by multiphonon states or transitions from these states, as they require higher-order scattering processes in order to lead to observable coherent phonons at the Brillouin-zone center [44,49].

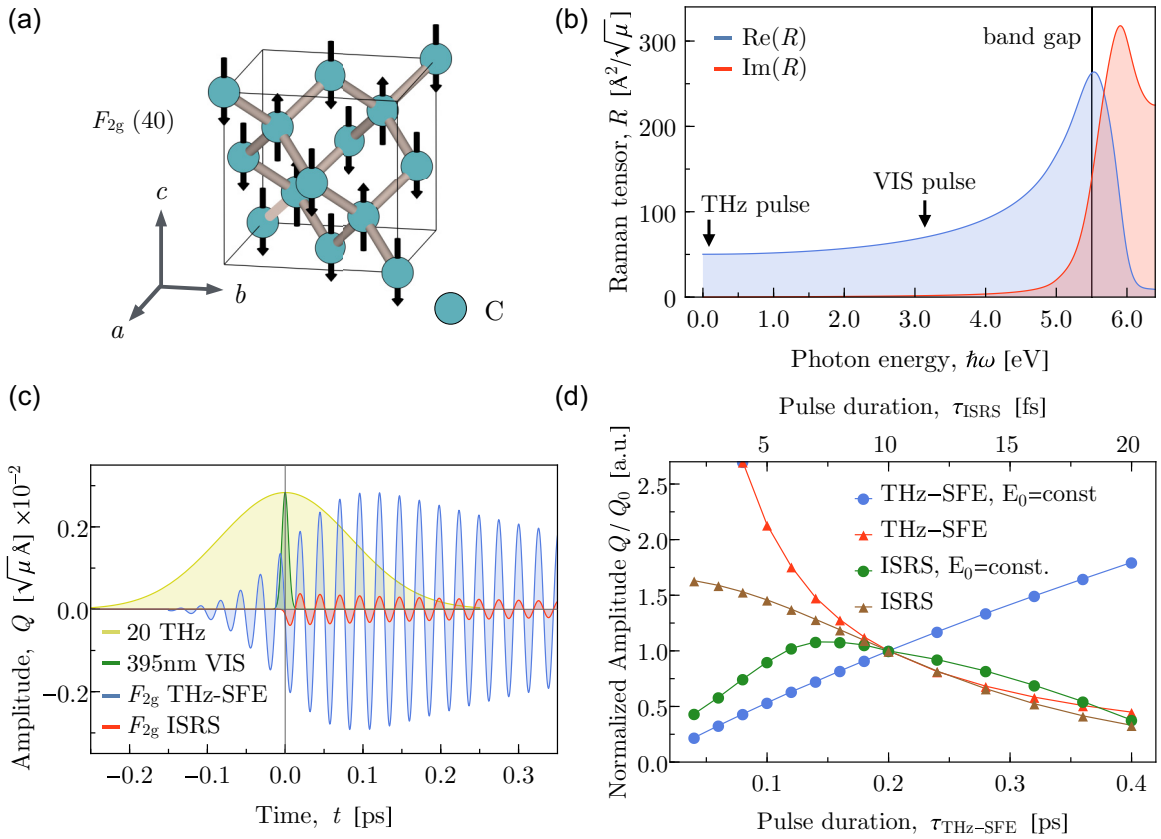

FIG. 2. (a) Eigenvector of the 40 THz F_{2g} mode of diamond. (b) Real and imaginary part of the single independent component of the Raman tensor. Black arrows mark the energies of the terahertz (20 THz ≡ 0.08 eV) and the visible light (395 nm ≡ 3.14 eV) pulse; the solid black line marks the band gap of diamond at 5.5 eV. (c) Evolution of the F_{2g} mode following THz-SFE and ISRS by a terahertz and visible light pulse, respectively. The envelopes of the excitation pulses are shown schematically. (d) Dependence of the normalized phonon amplitude Q/Q_0 on the duration of the terahertz and visible light pulse, $\tau_{THz\text{-}SFE}$ and τ_{ISRS}. Q_0 is the maximum phonon amplitude at $\tau_{THz\text{-}SFE} = 0.2$ ps and $\tau_{ISRS} = 10$ fs. We show two cases, one in which E_0 is kept constant while changing τ (circles), and one in which the total pulse energy is kept constant while changing τ and E_0 accordingly (triangles).

B. THz-SFE versus ionic Raman scattering in $ErFeO_3$

We will now compare THz-SFE to the conventional, difference-frequency type of ionic Raman scattering (DF-IRS) at the example of $ErFeO_3$. For orthorhombic $ErFeO_3$ with space group $Pnma$, experimental and theoretical studies are available that show the coupling of the Raman-active 3.2 THz A_g mode [see Fig. 3(a)], with the infrared-active 16.5 THz B_{3u} mode fulfilling the condition $\Omega_{IR} > \Omega_R$ [9,25]. Therefore, we model two different terahertz pulses, one with $\omega_0 = \Omega_R/2$ for THz-SFE according to Eq. (2), and the other to initially excite the B_{3u} mode for ionic Raman scattering according to Eqs. (3) and (4). The electric field for THz-SFE is oriented along the Raman-active c direction with a center frequency of $\omega_0/2\pi = 1.6$ THz and pulse duration of $\tau = 1$ ps; the electric field for DF-IRS is oriented along the infrared-active a direction with $\omega_0/2\pi = 16.5$ THz and $\tau = 0.2$ ps. We assume a peak electric field of $E_0 = 8$ MV/cm in both cases. The calculated parameters for the equations of motion are given in Table II, and the eigenvector of the A_g mode is illustrated in Fig. 3(a).

We show the resulting dynamics of the A_g mode after each optical excitation as described by Eqs. (2)–(4) in Fig. 3(b). As in the case of diamond, the response for THz-SFE shows a continuous increase of the phonon amplitude with the onset of the pulse, reaching a maximum of $Q = 2.6 \times 10^{-2}$ $\sqrt{\mu}$Å. The response for DF-IRS shows an impulsive onset of the phonon amplitude at $t = 0$ that is not sensitive to the carrier-envelope phase φ_{CEP} [46], as well as the typical displacive feature of nonlinear phononics [20,21,25]. In this case, the maximum phonon amplitude reaches $Q = 0.9 \times 10^{-2}$ $\sqrt{\mu}$Å.

The amplitude of the A_g mode induced by THz-SFE is higher than the amplitude induced by DF-IRS by a factor of 3. The excitation mechanisms are fundamentally different, however, and the decisive factors are the values of the Raman tensor R arising from a change in polarizability, and the coupling coefficient c arising from an anharmonic phonon potential. The comparison between the excitation strengths therefore has to be done for each material and phonon mode. Note that DF-IRS is mainly used because of its unipolar displacive feature.

C. Photonic and ionic sum-frequency excitation in $BiFeO_3$

In the previous sections we compared the recently demonstrated THz-SFE with the commonly used ISRS and DF-IRS. In this final step, we propose the so-far overlooked sum-frequency counterpart of ionic Raman scattering (SF-IRS) as depicted in Fig. 1(d). We demonstrate this mechanism and

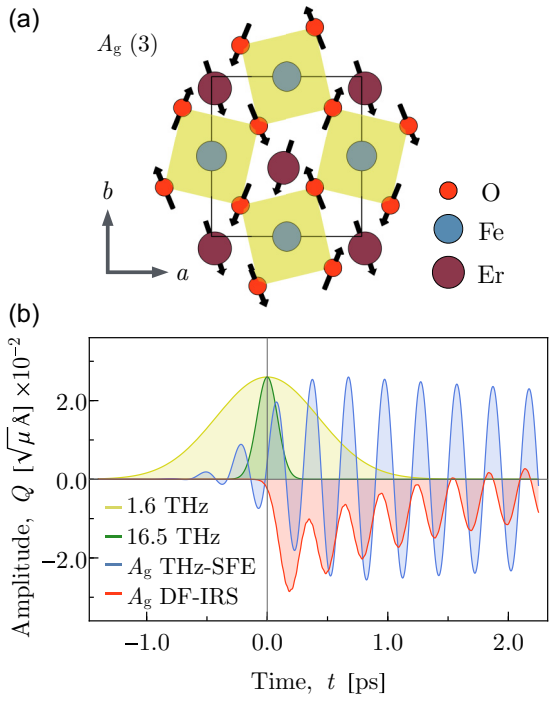

FIG. 3. (a) Eigenvector of the 3.2 THz A_g mode in the ab plane of orthorhombic $ErFeO_3$. The iron ions do not move in this mode. (b) Evolution of the A_g mode following THz-SFE and DF-IRS by a 1.6 and 16.5 THz pulse, respectively. The envelopes of the excitation pulses are shown schematically.

compare it to THz-SFE using the example of $BiFeO_3$. In noncentrosymmetric rhombohedral $BiFeO_3$ with space group $R3c$, all fully symmetric A_1 modes are both infrared active and Raman active along the [111] direction of the crystal. These modes couple quadratic linearly to each other, and two of them lie at frequencies of 15.3 and 7.4 THz [in the following referred to as $A_1(15)$ and $A_1(7)$ modes, respectively]. Thus by exciting the system with a single pulse with a center frequency of $\omega_0/2\pi = 7.6$ THz we expect both THz-SFE and SF-IRS to occur at the same time: The pulse directly excites the $A_1(7)$ mode via infrared absorption, which then mediates energy to the $A_1(15)$ mode via SF-IRS. Simultaneously, the pulse excites the $A_1(15)$ mode via THz-SFE [but not via infrared absorption as the $A_1(15)$ phonon lies well outside the 2.9 THz bandwidth of the pulse]. To make this process clearer, we show a schematic of the excitations in Fig. 4(a). Note that one could also drive the 15.3 THz mode directly via infrared absorption. For consistency to the previous sections, we label the 7.4 THz mode as "IR" and the 15.3 THz mode as "R," and both criteria, $\omega_0 \approx \Omega_R/2$ and $\Omega_{IR} \approx \Omega_R/2$, are fulfilled. We model the terahertz pulse with a center frequency of $\omega_0/2\pi = 7.6$ THz and a duration of $\tau = 0.3$ ps. The electric field is oriented along the Raman- and infrared-active [111] direction with a peak of $E_0 = 8$ MV/cm. The calculated parameters for the equations of motion are given in Table II, and the eigenvectors of the A_1 modes are illustrated in Fig. 4(b).

We show the resulting dynamics of both A_1 modes after the optical excitation as described by Eqs. (2)–(4) in Figs. 4(c) and 4(d). The response for the *simultaneous* excitation via THz-SFE and SF-IRS in Fig. 4(c) shows a fundamentally different behavior from the other three mechanisms: A beat signal arises and the phonon amplitude reaches by far the highest value of all three examples, $Q = 0.37\sqrt{\mu}$Å. We separate the effects of THz-SFE and SF-IRS in Fig. 4(d). The response for SF-IRS entirely captures the new feature, while the THz-SFE contribution leads only to a negligible increase of the phonon amplitude and phase shift. The beat signal is caused by a mutual exchange of energy between the infrared-active and Raman-active phonon, and the beat frequency is determined by the strength of the anharmonic phonon coupling c and through Q_R by the strength of the terahertz pulse [see Eq. (3)]. A node of the beat signal of the $A_1(15)$ mode corresponds to a maximum of the modulation of the $A_1(7)$ mode [see black arrows in Fig. 4(c)]. The maximum is mostly swallowed by the damping, however. Naturally, for sum-frequency excitation, the phase of the response is sensitive to the carrier-envelope phase of the terahertz pulse φ_{CEP} [46]. Higher-order anharmonicities in the potential $V(Q_R, Q_{IR})$ affect the amplitude, beat frequency, and even introduce new beats, however, to a much smaller degree than the quadratic-linear coupling $Q_{IR}^2 Q_R$ [46].

IV. DISCUSSION

We completed the map of photonic and ionic Raman scattering for the excitation of Raman-active phonons in insulators with the missing sum-frequency part of ionic Raman scattering [see Fig. 1(d)]. The difference-frequency mechanisms are impulsive in nature and not sensitive to the carrier-envelope phase of the driving field φ_{CEP}, whereas the sum-frequency mechanisms are nonimpulsive and therefore sensitive to φ_{CEP}. A summary of the properties is shown in Table I.

Among the investigated phonon excitations, the up-conversion of frequency components of the driving force is more efficient than the down-conversion. An increase of the total pulse energy will only enhance the difference-frequency excitation if it is due to a higher peak electric field E_0, but not due to a longer pulse duration τ. In contrast, an increase of either E_0 or τ leads to a stronger sum-frequency excitation. This property is particularly relevant for narrow-band excitation pulses, for example, generated by accelerator-based midinfrared and terahertz sources [3,50,51]. The resulting frequency components are weighted by the Raman tensor and anharmonic phonon coupling, which both depend on the material properties.

For homonuclear materials that do not possess infrared-active phonons, such as diamond, only photonic difference- and sum-frequency excitation is possible. Here, the more efficient conversion of sum-frequency components also leads to a higher selectivity for THz-SFE compared to ISRS. Generally, the selectivity depends on the symmetries and frequencies of the phonon modes in the material. In the photonic Raman mechanisms the electric field has to be oriented along the Raman-active direction of the target Q_R mode, while in the ionic Raman mechanisms it has to be oriented along the infrared-active direction of the coupling Q_{IR} mode. Consequently, the selectivity depends on whether "unwanted" phonon modes lie within the bandwidth and polarization direction of the driving force $E(t)$ (infrared active) or $E^2(t)$ (Raman active) in addition to our target Q_{IR} and Q_R modes. For lattice-driven phenomena in the electronic ground state,

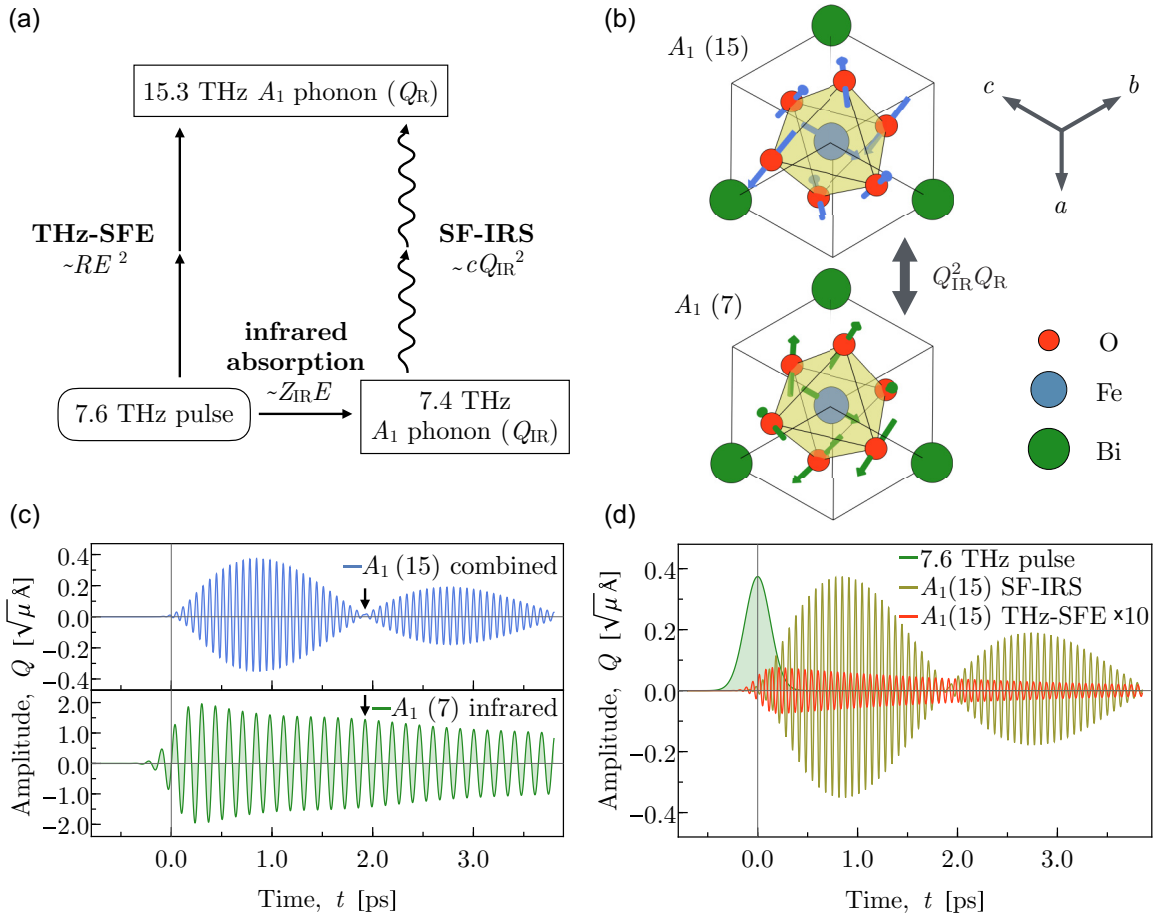

FIG. 4. (a) Schematic of the excitation by the terahertz pulse. (b) Eigenvectors of the coupled 15.3 THz (blue) and 7.4 THz (green) A_1 modes from a view along the [111] direction of rhombohedral $BiFeO_3$. The motion of bismuth ions in these modes is negligible. (b) Full evolution of the A_1 modes following the excitation by a single 7.6 THz pulse. The $A_1(7)$ mode is excited via infrared absorption. The $A_1(15)$ mode is excited *simultaneously* via THz-SFE and SF-IRS. Black arrows point to the beat nodes of the $A_1(15)$ mode that correspond to maxima of the modulation of the $A_1(7)$ mode. (c) Evolution of the $A_1(15)$ mode as in (b), but separating the effects of the two mechanisms. The marginal THz-SFE contribution is magnified by a factor of ten for better visibility. The envelope of the excitation pulse is shown schematically.

all three terahertz excitation mechanisms, THz-SFE, DF-IRS, and SF-IRS, are favorable over commonly used visible-light or near-infrared ISRS in order to avoid parasitic electronic excitations. The sum-frequency processes provide an additional route to excite optical phonons in the range of 5–15 THz, for which powerful sources are only now becoming feasible [3,52]. Recent advances in nonoptical probing techniques, such as ultrafast electron diffraction, and diffuse x-ray and electron scattering [53–56], will further improve the analysis of coupled lattice dynamics, complementary to established methods [57,58].

With the increased availability of strong terahertz and midinfrared sources, we anticipate that the presented map of photonic and ionic Raman mechanisms will serve as a guide for the selective excitation of crystal lattice vibrations in the future. Specifically, we expect that the strong excitation of Raman-active phonons will complement the effects arising from infrared-active phonons in the context of spin-phonon and electron-phonon coupled phenomena.

ACKNOWLEDGMENTS

We thank M. Fechner, T. Kampfrath, Q. Meier, R. Merlin, M. Wolf, A. Paarmann, X.-Y. Zhu, and N. Spaldin for useful discussions and support. This work was funded by the ETH Zürich and ERC-H2020 Grant TERAMAG/No. 681917 (to T. Kampfrath). The work at Columbia University was supported by Office of Naval Research Grant No. 01-N00014-18-1-2080 (to X.-Y. Zhu). Calculations were performed at the Swiss National Supercomputing Centre (CSCS) supported by the Project IDs No. s624 and No. p504.

[1] D. M. Juraschek and N. A. Spaldin, Sounding out optical phonons, Science **357**, 873 (2017).

[2] T. Kampfrath, K. Tanaka, and K. A. Nelson, Resonant and nonresonant control over matter and light by intense terahertz transients, Nat. Photonics **7**, 680 (2013).

[3] S. S. Dhillon, M. S. Vitiello, E. H. Linfield, A. G. Davies, M. C. Hoffmann, J. Booske, C. Paoloni, M. Gensch, P. Weightman, G. P. Williams, E. Castro-Camus, D. R. S. Cumming, F. Simoens, I. Escorcia-Carranza, J. Grant, S. Lucyszyn, M. Kuwata-Gonokami, K. Konishi, M. Koch, C. A. Schmuttenmaer *et al.*, The 2017 terahertz science and technology roadmap, J. Phys. D: Appl. Phys. **50**, 043001 (2017).

[4] A. Sell, A. Leitenstorfer, and R. Huber, Phase-locked generation and field-resolved detection of widely tunable terahertz pulses with amplitudes exceeding 100 MV/cm, Opt. Lett. **33**, 2767 (2008).

[5] M. Rini, R. Tobey, N. Dean, J. Itatani, Y. Tomioka, Y. Tokura, R. W. Schoenlein, and A. Cavalleri, Control of the electronic phase of a manganite by mode-selective vibrational excitation, Nature (London) **449**, 72 (2007).

[6] D. Fausti, R. I. Tobey, N. Dean, S. Kaiser, A. Dienst, M. C. Hoffmann, S. Pyon, T. Takayama, H. Takagi, and A. Cavalleri, Light-induced superconductivity in a stripe-ordered cuprate, Science **331**, 189 (2011).

[7] W. Hu, S. Kaiser, D. Nicoletti, C. R. Hunt, I. Gierz, M. C. Hoffmann, M. Le Tacon, T. Loew, B. Keimer, and A. Cavalleri, Optically enhanced coherent transport in $YBa_2Cu_3O_{6.5}$ by ultrafast redistribution of interlayer coupling, Nat. Mater. **13**, 705 (2014).

[8] M. Mitrano, A. Cantaluppi, D. Nicoletti, S. Kaiser, A. Perucchi, S. Lupi, P. Di Pietro, D. Pontiroli, M. Riccò, S. R. Clark, D. Jaksch, and A. Cavalleri, Possible light-induced superconductivity in K_3C_{60} at high temperature, Nature (London) **530**, 461 (2016).

[9] T. F. Nova, A. Cartella, A. Cantaluppi, M. Först, D. Bossini, R. V. Mikhaylovskiy, A. V. Kimel, R. Merlin, and A. Cavalleri, An effective magnetic field from optically driven phonons, Nat. Phys. **13**, 132 (2017).

[10] S. Maehrlein, I. Radu, P. Maldonado, A. Paarmann, M. Gensch, A. M. Kalashnikova, R. V. Pisarev, M. Wolf, P. M. Oppeneer, J. Barker, and T. Kampfrath, Revealing spin-phonon interaction in ferrimagnetic insulators by ultrafast lattice excitation, arXiv:1710.02700.

[11] T. Dekorsy, G. C. Cho, and H. Kurz, Coherent phonons in condensed media, in *Light Scattering in Solids VIII*, edited by M. Cardona and G. Güntherodt, Topics in Applied Physics Vol. 76 (Springer, Berlin, 2000), pp. 169–209.

[12] M. Först and T. Dekorsy, Coherent phonons in bulk and low-fimensional semiconductors, in *Coherent Vibrational Dynamics*, edited by S. De Silvestri, G. Cerullo, and G. Lanzani (Taylor & Francis, London, 2008), pp. 129–172.

[13] Under photoexcitation there are a lot more mechanisms that excite Raman-active phonons, such as "displacive excitation of coherent phonons" or "transient depletion field screening," for example.

[14] S. De Silvestri, J. G. Fujimoto, E. P. Ippen, E. B. Gamble, Jr., L. R. Williams, and K. A. Nelson, Femtosecond time-resolved measurements of optic phonon dephasing by impulsive stimulated Raman scattering in α-perylene crystal from 20 to 300 K, Chem. Phys. Lett. **116**, 146 (1985).

[15] R. Merlin, Generating coherent THz phonons with light pulses, Solid State Commun. **102**, 207 (1997).

[16] T. E. Stevens, J. Kuhl, and R. Merlin, Coherent phonon generation and the two stimulated Raman tensors, Phys. Rev. B **65**, 144304 (2002).

[17] A. A. Maradurin and R. F. Wallis, Ionic Raman effect. I. Scattering by localized vibration modes, Phys. Rev. B **2**, 4294 (1970).

[18] R. F. Wallis and A. A. Maradurin, Ionic Raman effect. II. The first-order ionic Raman effect, Phys. Rev. B **3**, 2063 (1971).

[19] L. B. Humphreys, Ionic Raman effect. III. First- and second-order ionic Raman effects, Phys. Rev. B **6**, 3886 (1972).

[20] M. Först, C. Manzoni, S. Kaiser, Y. Tomioka, Y. Tokura, R. Merlin, and A. Cavalleri, Nonlinear phononics as an ultrafast route to lattice control, Nat. Phys. **7**, 854 (2011).

[21] A. Subedi, A. Cavalleri, and A. Georges, Theory of nonlinear phononics for coherent light control of solids, Phys. Rev. B **89**, 220301 (2014).

[22] D. Nicoletti and A. Cavalleri, Nonlinear light–matter interaction at terahertz frequencies, Adv. Opt. Photonics **8**, 401 (2016).

[23] S. Maehrlein, A. Paarmann, M. Wolf, and T. Kampfrath, Terahertz Sum-Frequency Excitation of a Raman-Active Phonon, Phys. Rev. Lett. **119**, 127402 (2017).

[24] X. Gonze and C. Lee, Dynamical matrices, Born effective charges, dielectric permittivity tensors, and interatomic force constants from density-functional perturbation theory, Phys. Rev. B **55**, 10355 (1997).

[25] D. M. Juraschek, M. Fechner, and N. A. Spaldin, Ultrafast Structure Switching through Nonlinear Phononics, Phys. Rev. Lett. **118**, 054101 (2017).

[26] L. Dhar, J. A. Rogers, and K. A. Nelson, Time-resolved vibrational spectroscopy in the impulsive limit, Chem. Rev. **94**, 157 (1994).

[27] A. Subedi, Proposal for ultrafast switching of ferroelectrics using midinfrared pulses, Phys. Rev. B **92**, 214303 (2015).

[28] M. Fechner and N. A. Spaldin, Effects of intense optical phonon pumping on the structure and electronic properties of yttrium barium copper oxide, Phys. Rev. B **94**, 134307 (2016).

[29] A. Subedi, Midinfrared-light-induced ferroelectricity in oxide paraelectrics via nonlinear phononics, Phys. Rev. B **95**, 134113 (2017).

[30] R. Mankowsky, A. von Hoegen, M. Först, and A. Cavalleri, Ultrafast Reversal of the Ferroelectric Polarization, Phys. Rev. Lett. **118**, 197601 (2017).

[31] M. Gu and J. M. Rondinelli, Role of orbital filling on nonlinear ionic Raman scattering in perovskite titanates, Phys. Rev. B **95**, 024109 (2017).

[32] M. Gu and J. M. Rondinelli, Nonlinear phononic control and emergent magnetism in correlated titanates, arXiv:1710.00993.

[33] M. Fechner, A. Sukhov, L. Chotorlishvili, C. Kenel, J. Berakdar, and N. A. Spaldin, Magnetophononics: Ultrafast spin control through the lattice, arXiv:1707.03216.

[34] A. P. Itin and M. I. Katsnelson, Efficient excitation of nonlinear phonons via chirped mid-infrared pulses: Induced structural phase transitions, arXiv:1707.02455.

[35] G. Kresse and J. Furthmüller, Efficiency of *ab initio* total energy calculations for metals and semiconductors using a plane-wave basis set, Comput. Mater. Sci. **6**, 15 (1996).

[36] G. Kresse and J. Furthmüller, Efficient iterative schemes for *ab initio* total-energy calculations using a plane-wave basis set, Phys. Rev. B **54**, 11169 (1996).

[37] A. Togo and I. Tanaka, First principles phonon calculations in materials science, Scr. Mater. **108**, 1 (2015).

[38] D. Porezag and M. R. Pederson, Infrared intensities and Raman-scattering activities within density-functional theory, Phys. Rev. B **54**, 7830 (1996).

[39] H. J. Monkhorst and J. D. Pack, Special points for Brillouin-zone integrations, Phys. Rev. B **13**, 5188 (1976).

[40] G. I. Csonka, J. P. Perdew, A. Ruzsinszky, P. H. T. Philipsen, S. Lebègue, J. Paier, O. A. Vydrov, and J. G. Ángyán, Assessing the performance of recent density functionals for bulk solids, Phys. Rev. B **79**, 155107 (2009).

[41] C. Ederer and N. A. Spaldin, Weak ferromagnetism and magnetoelectric coupling in bismuth ferrite, Phys. Rev. B **71**, 060401(R) (2005).

[42] L. Wei, S. Fan, X. P. Wang, B. Liu, Y. Y. Zhang, X. S. Lv, Y. G. Yang, H. J. Zhang, and X. Zhao, Lattice dynamics of bismuth-deficient $BiFeO_3$ from first principles, Comput. Mater. Sci. **111**, 374 (2016).

[43] I. Sosnowska, W. Schäfer, W. Kockelmann, K. H. Andersen, and I. O. Troyanchuk, Crystal structure and spiral magnetic ordering in $BiFeO_3$ doped with manganese, Appl. Phys. A **74**, S1040 (2002).

[44] R. P. Mildren and J. R. Rabeau, *Optical Engineering of Diamond* (Wiley, Hoboken, NJ, 2013).

[45] K. Ishioka, M. Hase, K. Masahiro, and H. Petek, Coherent optical phonons in diamond, Appl. Phys. Lett. **89**, 231916 (2016).

[46] See Supplemental Material at http://link.aps.org/supplemental/10.1103/PhysRevB.97.174302 for illustrations of phase sensitivity, central-frequency dependence, and higher-order anharmonic couplings.

[47] Y. Shinohara, K. Yabana, Y. Kawashita, J.-I. Iwata, T. Otobe, and G. F. Bertsch, Coherent phonon generation in time-dependent density functional theory, Phys. Rev. B **82**, 155110 (2010).

[48] Y. Shinohara, Y. Kawashita, J.-I. Iwata, K. Yabana, T. Otobe, and G. F. Bertsch, First-principles description for coherent phonon generation in diamond, J. Phys.: Condens. Matter **22**, 384212 (2010).

[49] M. E. Thomas, Multiphonon model for absorption in diamond, Proc. SPIE **2286**, 152 (1994).

[50] B. Green, S. Kovalev, V. Asgekar, G. Geloni, U. Lehnert, T. Golz, M. Kuntzsch, C. Bauer, J. Hauser, J. Voigtlaender, B. Wustmann, I. Koesterke, M. Schwarz, M. Freitag, A. Arnold, J. Teichert, M. Justus, W. Seidel, C. Ilgner, N. Awari *et al.*, High-field high-repetition-rate sources for the coherent THz control of matter, Sci. Rep. **6**, 22256 (2016).

[51] P. Gruene, D. M. Rayner, B. Redlich, A. F. G. van der Meer, J. T. Lyon, G. Meijer, and A. Fielicke, Structures of neutral Au_7, Au_{19}, and Au_{20} clusters in the gas phase, Science **321**, 674 (2008).

[52] B. Liu, H. Bromberger, A. Cartella, T. Gebert, M. Först, and A. Cavalleri, Generation of narrowband, high-intensity, carrier-envelope phase-stable pulses tunable between 4 and 18 THz, Opt. Lett. **42**, 129 (2017).

[53] D. Zhu, A. Robert, T. Henighan, H. T. Lemke, M. Chollet, J. M. Glownia, D. A. Reis, and M. Trigo, Phonon spectroscopy with sub-meV resolution by femtosecond x-ray diffuse scattering, Phys. Rev. B **92**, 054303 (2015).

[54] L. Waldecker, T. Vasileiadis, R. Bertoni, R. Ernstorfer, T. Zier, F. H. Valencia, M. E. Garcia, and E. S. Zijlstra, Coherent and incoherent structural dynamics in laser-excited antimony, Phys. Rev. B **95**, 054302 (2017).

[55] M. J. Stern, L. P. René de Cotret, M. R. Otto, R. P. Chatelain, J.-P. Boisvert, M. Sutton, and B. J. Siwick, Mapping momentum-dependent electron-phonon coupling and nonequilibrium phonon dynamics with ultrafast electron diffuse scattering, Phys. Rev. B **97**, 165416 (2018).

[56] S. W. Teitelbaum, T. Henighan, Y. Huang, H. Liu, M. P. Jiang, D. Zhu, M. Chollet, T. Sato, É. D. Murray, S. Fahy, S. O'Mahony, T. P. Bailey, C. Uher, M. Trigo, and D. A. Reis, Direct measurement of anharmonic decay channels of a coherent phonon, arXiv:1710.02207.

[57] K. Sokolowski-Tinten, C. Blome, J. Blums, A. Cavalleri, C. Dietrich, A. Tarasevitch, I. Uschmann, E. Förster, M. Kammler, M. Horn-von Hoegen, and D. von der Linde, Femtosecond x-ray measurement of coherent lattice vibrations near the Lindemann stability limit, Nature (London) **422**, 287 (2003).

[58] M. Bargheer, N. Zhavoronkov, Y. Gritsai, J. C. Woo, D. S. Kim, M. Woerner, and T. Elsaesser, Coherent atomic motions in a nanostructure studied by femtosecond x-ray diffraction, Science **306**, 1771 (2004).